HgTe Nanocrystal-Based Photodiode for Extended Short-Wave Infrared Sensing with Optimized Electron Extraction and Injection

Charlie Gréboval, Eva Izquierdo, Claire Abadie, Adrien Khalili, Mariarosa Cavallo, Audrey Chu, Tung Huu Dang, Huichen Zhang, Xavier Lafosse, Michael Rosticher, et al.

To cite this version:

Charlie Gréboval, Eva Izquierdo, Claire Abadie, Adrien Khalili, Mariarosa Cavallo, et al.. HgTe Nanocrystal-Based Photodiode for Extended Short-Wave Infrared Sensing with Optimized Electron Extraction and Injection. ACS Applied Nano Materials, In press, 10.1021/acsanm.2c02103 . hal-03694576

HAL Id: hal-03694576
https://hal.science/hal-03694576v1

HgTe Nanocrystal-Based Photodiode for Extended Short Wave Infrared Sensing with Optimized Electron Extraction and Injection

Charlie Gréboval[1], Eva Izquierdo[1], Claire Abadie[1], Adrien Khalili[1], Mariarosa Cavallo[1], Audrey Chu[1], Tung Huu Dang[1], Huichen Zhang[1], Xavier Lafosse[2], Michael Rosticher[3], Xiang Zhen Xu[4], Armel Decamps-Mandine[5], Abdelkarim Ouerghi[2], Mathieu G. Silly[6], Sandrine Ithurria[4], Emmanuel Lhuillier[1*]

[1] Sorbonne Université, CNRS, Institut des NanoSciences de Paris, INSP, F-75005 Paris, France.
[2] Université Paris-Saclay, CNRS, Centre de Nanosciences et de Nanotechnologies, CNRS, 10 Boulevard Thomas Gobert, 91120 Palaiseau, France
[3] Laboratoire de Physique de l'Ecole normale supérieure, ENS, Université PSL, CNRS, Sorbonne Université, Université Paris-Diderot, Sorbonne Paris Cité, Paris, France Paris.
[4] Laboratoire de Physique et d'Etude des Matériaux, ESPCI-Paris, PSL Research University, Sorbonne Université Univ Paris 06, CNRS UMR 8213, 10 rue Vauquelin 75005 Paris, France.
[5] Centre de MicroCaractérisation Raimond Castaing, UAR3623, CNRS, Université de Toulouse, 3 rue Caroline Aigle, 31400 Toulouse, France
[6] Synchrotron-SOLEIL, Saint-Aubin, BP48, F91192 Gif sur Yvette Cedex, France.

Abstract: Thanks to their narrow band gap nature and fairly high carrier mobility, HgTe nanocrystals are of utmost interest for optoelectronics beyond the telecom window (λ>1.55 µm). In particular, they offer an interesting cost-effective alternative to the well-developed InGaAs technology. However, in contrast to PbS, far less work has been dedicated to the integrating this material in photodiodes. In the short-wave infrared, HgTe NCs have a more *p*-type character than in the mid wave infrared, thus promoting the development of new electron transport layers with an optimized band alignment. As for perovskites, HgTe NCs present a fairly deep band gap with respect to vacuum. Thus, we were motivated by the strategy developed for perovskite solar cells, for which SnO_2 has led to the best performing devices. Here, we explore the following stack made of SnO_2/HgTe/Ag_2Te in which the SnO_2 and Ag_2Te layers behave as electron and hole extractors respectively. Using X-ray photoemission, we show that SnO_2 presents a nearly optimal band alignment with HgTe to efficiently filter the hole dark current while letting the photoelectrons flow. The obtained I-V curve exhibits an increased rectifying behavior, and the diode stack presents a high internal efficiency for the diode (above 60%) and an external quantum efficiency that is mostly limited by the absorption magnitude. Furthermore, we tackle a crucial challenge for the transfer of such diode onto readout circuits which prevents back-side illumination. We also demonstrate that the diode stack is reversible with a partly transparent conducting electrode on top while preserving the device's responsivity. Finally, we show that such SnO_2 layer is also beneficial for electron injection and leads to enhanced electroluminescent signal as the diode is operated under forward bias. This work is an essential step toward the design of a focal plane array with an HgTe NCs-based photodiode.

Keywords: short wave infrared, detection, HgTe, nanocrystals, photodiode

*To whom correspondence should be sent: el@insp.upmc.fr

INTRODUCTION

Thanks to their cost-effective fabrication, nanocrystals (NCs)[1] raise interest in the design of optoelectronic devices. This is especially true in the spectral range where silicon cannot be used and for which alternative materials, generally epitaxially grown semiconductors, have to be integrated. This is typically the case of infrared, a spectral range where the device cost is prohibitive for many applications[2]. Over the past decade, significant progresses have been made on integrating NCs at the focal plane array (FPA) level.[3–7] Lead sulfide NCs have reached the global market, but the spectral range of this material mostly overlaps that of existing InGaAs technology. HgTe nanocrystals[8–11], with their even narrower band gap, open up a new degree of freedom to explore longer wavelengths[12], at least up to mid-wave infrared and possibly even further in the THz range.[13–15] However, HgTe-based devices are still in their early stage of development. In particular, there are only a few studies dedicated to photodiode structures that have been reported.[16–18] The Heiss' group proposed a diode stack inspired by solar cells where the absorbing HgTe layer is coupled to a TiO_2 electron transport layer (ETL).[17] The resulting device presents a rectifying I-V curve, but the photocurrent was modest because of the poor band alignment between the two materials, so that TiO_2 also filters the photoelectrons, as later shown by Jagtap et al. [19,20]

In the mid-wave infrared (MWIR), Ackerman *et al.*[18] introduced a hole transport layer based on a Hg cation exchanged layer of Ag_2Te NC. The efficiency of this layer in the MWIR is related to the *n*-type nature of HgTe NCs in this spectral range. As a result, an efficient *pn* junction is formed at the HgTe/Ag_2Te interface. When shorter wavelengths are targeted, HgTe acquires a more *p*-type[20] character, and thus the HgTe-Ag_2Te junction is mostly a *p-p'* junction. This leads to a drop in performance for wavelengths below 2.5 µm[21] (short wave infrared or SWIR range). A possible strategy is to introduce a gate at the level of the electron extracting electrode[22], but such an approach is technologically demanding and difficult to implement at the FPA level. Tang *et al.* proposed to use Bi_2Se_3 flakes as an electron transport layer[23]; however, the large lateral extension of the flakes makes it difficult to build a pinhole-free film from this material. Recently Khalili *et al* have proposed an original diode design based on HgTe NCs coupled to epitaxially grown InGaAs wires used as electron extractor, however this approach loses the benefit of the solution processability. [24]

It is important to stress that all reported diode stacks terminate with a metallic mirror. While such strategy is compatible with back-side illumination, it is incompatible with the presence of a readout integrated circuit (ROIC). Thus, it is of utmost interest to develop a new carrier extraction layer that matches the constraints raised by narrow band gap materials and enables a reversed fabrication. To design an efficient electron transport layer (ETL) that aims to be coupled with a SWIR absorbing HgTe NCs, the following constraints have to be fulfilled: (*i*) the conduction band has to be resonant with the one of the absorbing layer, (*ii*) the valence band has to be strongly offset to prevent hole dark current injection. Both constraints imply that the band gap of this layer has to be significantly larger than the one of the absorbing layer, (*iii*) the material has to be *n-type* to prevent further hole injection, (*iv*) the material should be processable at a fairly low temperature to avoid any sintering of the HgTe NCs. The latter process will shift the cut-off wavelength while increasing the dark current. Lastly, (*v*) the top contact has to be (partly) transparent to be ROIC compatible.

Infrared absorbing mercury chalcogenides NCs[8] combine a narrow band gap nature with a fairly large work function of the bulk material.[25] This makes the conduction band fairly deep with respect to the vacuum level. This observation explains why TiO_2 is a sub-optimal ETL for HgTe NC-based diodes. Interestingly, the same issue is faced by perovskite materials used in solar cells. As a result, a large interest has been focused on tin oxide.[26–31] SnO_2 presents a deeper band gap with respect to the vacuum level compared to other oxide materials such as ZnO or TiO_2. In this paper, we study the potential of SnO_2 as ETL coupled to HgTe NCs for SWIR sensing. We demonstrate, using photoemission, that SnO_2 presents a nearly optimal band alignment with HgTe with a resonant conduction band. We then conduct a deep structural investigation of the diode stack and identify the optimal thickness to maximize the absorption. An interesting feature of this diode is the lack of *1/f* noise[32,33], which is generally prevailing in most devices based on NCs. In the final part of the paper, we demonstrate that the diode stack is compatible with a reversed contact while maintaining most of the performance. This result is an important step toward the transfer of the diode onto focal plane arrays. Finally, we also text the benefit of this ETL for charge injection as the diode is used as a light emitting diode and show an increase of the relative EQE of almost a factor 10.

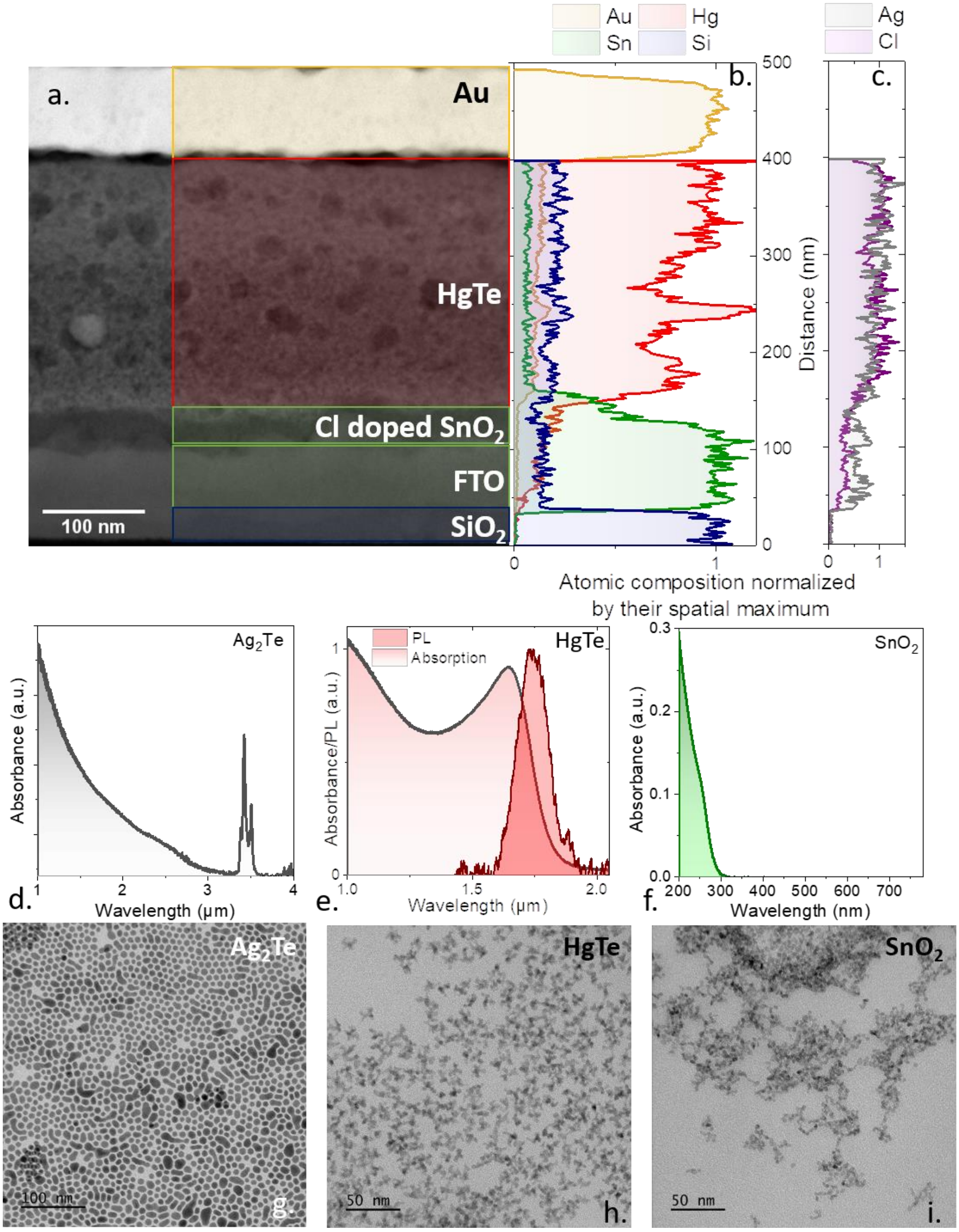

***Figure 1 Diode structural properties**. a. Transmission electron microscopy image of the FTO/ doped:SnO_2/HgTe/Ag_2Te/Au stack. False colors have been superimposed. b. (resp c.) Signal from EDX normalized by the value at their maximum for Au, Hg, Sn and Si (resp. Ag and Cl). d. (resp g.) Absorption spectrum (resp. TEM image) of Ag_2Te NCs. e. (resp h.) Absorption and photoluminescence (resp TEM image) of HgTe NCs. f. (resp i.) Absorption spectrum (resp TEM image) of SnO_2 NCs.*

DISCUSSION AND RESULTS

To study the potential of SnO_2 as an electron transport layer coupled to HgTe NCs absorbing in the short-wave infrared, we start by fabricating a diode based on the following stack glass/FTO/doped SnO_2/HgTe/Ag_2Te/gold, where FTO stands for fluorine-doped tin oxide. This layer is a conventional transparent conductive oxide prepared by chemical vapor deposition. A moderate thickness of 80 nm is chosen to avoid excessive absorption in the short-wave infrared range.

The absorbing layer is made of HgTe NCs grown using the Keuleyan's procedure.[34] Transmission electron microscopy (TEM) can be seen in **Figure 1**h, and it shows a branched aspect for the particles. The HgTe NCs present a band edge at 1.7 µm (0.72 eV) according to absorption and photoluminescence spectra (**Figure 1**e). Following ligand exchange and thin-film processing, the band edge will shift to bring the cut-off wavelength around 2 µm, as later discussed. The top part of the diode is made of Hg cation exchanged Ag_2Te NCs behaving as a hole extracting layer as proposed by Ackerman *et al.*[18] The 8-10 nm Ag_2Te NCs (see TEM in **Figure 1**g) also present a narrow band gap nature and their infrared absorption spectrum displays a cut-off around 3 µm, see **Figure 1**d. For the ETL layer, we use commercially available SnO_2 particles (see **Figure 1**i for TEM) that are later doped on the surface using NH_4Cl. The formation of this layer follows the one developed for perovskites solar cells by the Reiss' group.[26] Their absorption spectrum shows a cut-off wavelength at around 300 nm corresponding to a band gap of 4.07 eV, see **Figure 1**f and S6. This layer is only annealed at 70 °C to dry the water used as a solvent. TEM and energy dispersive X-ray spectroscopy on the side of the diode enable a clear identification of the different layers, see **Figure 1**a-c. While Sn, Hg, and Au are forming well-identified layers, with no noticeable interdiffusion, the Cl (**Figure 1**c) is located all over the structure, consistent with its use as a capping ligand for both SnO_2 and HgTe layers. More surprisingly, and in spite of the thin character of the Ag_2Te layer (20-30 nm), the EDX profile suggests that Ag atoms diffuse all over the film thickness, as suggested by Ackerman *et al.*[18]

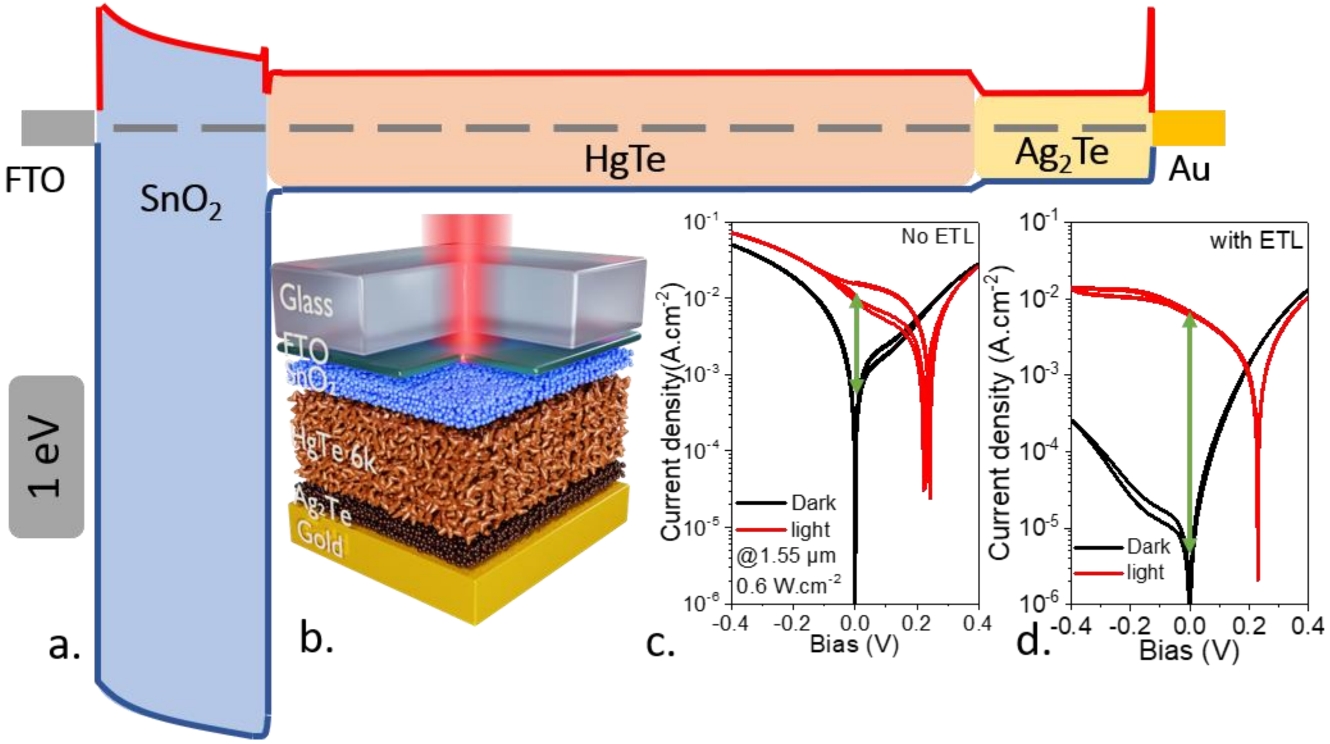

Figure 2* *Diode electronic structure. *a. Band diagram of the FTO/doped:SnO_2/HgTe/Ag_2Te/Au stack as revealed from photoemission. b Schematic of the diode stack: FTO/doped:SnO_2/HgTe/Ag_2Te/Au. c. I-V curves in the dark and under illumination (λ=1.55 µm – 0.6 $W.cm^{-2}$) for an FTO/HgTe/Ag_2Te/Au stack. d. I-V curves in the dark and under illumination (λ=1.55 µm – 0.6 $W.cm^{-2}$) for an FTO/ doped:SnO_2/HgTe/Ag_2Te/Au stack.*

The benefit for this specific diode stack, whose schematic is shown in **Figure 2**b and S5, is better revealed by determining its band alignment throughout X-ray photoemission, see Figure S2-3 for photoemission measurements and **Figure 2**a for the diode band structure. Interestingly, the band alignment is close to the targeted one with a quasi-resonant conduction band between doped SnO_2 and HgTe NCs, while the wide band gap of SnO_2 ensures a large offset of the valence band and thus an efficient dark hole current filtering. We also checked using field-effect-transistor measurements (Figure S4) that the SnO_2 layer only presents electron conduction.

To further understand the value of the ETL layer, we fabricated two diodes, one with and one without. Their I-V characteristics are given in **Figure 2**d and c, respectively. In the absence of the ETL layer, the dark I-V curve is barely rectifying at room temperature, in particular in the case of thick HgTe layer. However, under illumination, a clear open-circuit voltage can be observed, see **Figure 2**c. Note, that the curve presents some hysteresis that is likely due to the presence of free ions coming from the ligand exchange procedure. In the presence of the SnO_2 layer (**Figure 2**d), the I-V curve displays a genuine rectifying behavior, with two orders of magnitude for the current asymmetry between forward and reverse operation. We observe As a result, the photoinduced current modulation is drastically increased by two orders of magnitude for the zero-bias operation of the diode.

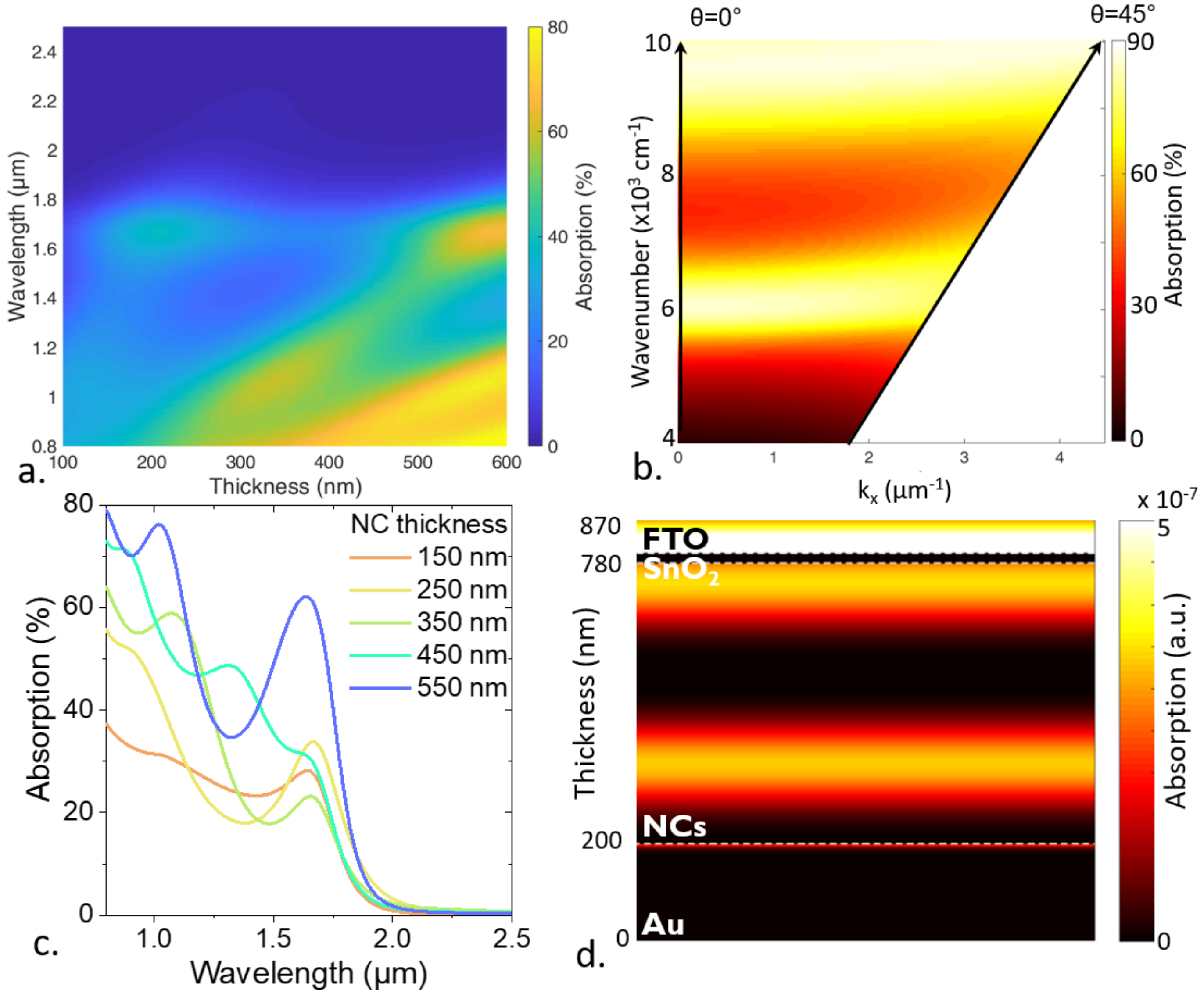

***Figure 3 Absorption within the FTO/doped:SnO_2/HgTe/Ag_2Te/Au stack**. a. Simulated absorption map in NCs only (i.e., excluding losses in contacts) as a function of the wavelength and thickness of the HgTe layer. b. Dispersion map (absorption as a function of in plane wavevector and total wavevector) for the diode stack for a 550 nm thickness of the HgTe layer. c. Absorption spectra of the diode for various thicknesses of the HgTe layer. d. Spatial map of the absorption of the diode stack for a 550 nm thickness of the HgTe layer*

Beyond the band alignment, the device absorption is another parameter driving the diode stack performance through the control of the layer thickness. Using rigorous coupled-wave analysis (RCWA), we simulate the device absorption properties. The inputs of these simulations are the complex optical index of each layer measured by ellipsometry, see Figure S9. **Figure 3**a shows the absorption spectra for various thicknesses of the HgTe layer. Note that in this graph, we only simulate the absorption occurring in the NC (*i.e.,* excluding the losses in metals) since only this contribution leads to the generation of photocurrent. We distinguish at λ=1.7 µm a stronger absorbing feature that can be associated with the band edge of the HgTe NCs. We also observe a series of tilted lines corresponding to various resonances of the absorption. The nature of these resonances is better revealed by the dispersion map, see **Figure 3**b. All features appear dispersion-less which is consistent with the formation of a Fabry-Pérot cavity. This mode leads to the formation of standing waves in the NC film, as shown on the absorption map, see **Figure 3**d. However, obtaining a significant absorption (above 50% at the band edge) requires the formation of fairly thick films above 500 nm for the HgTe layer, see **Figure 3**a and c. From a previous study, it has been demonstrated that such thick films are difficult to fabricate and may not lead to the best performance (in particular, high V_{OC}) due to the presence of pinholes. For a more typical thickness of 250 nm (see **Figure 1**a), the absorption is more in the 30-35% range, which is still higher than the value obtained for a free-standing layer of HgTe NC with the same thickness. This depicts the cavity effect resulting from the diode stack.

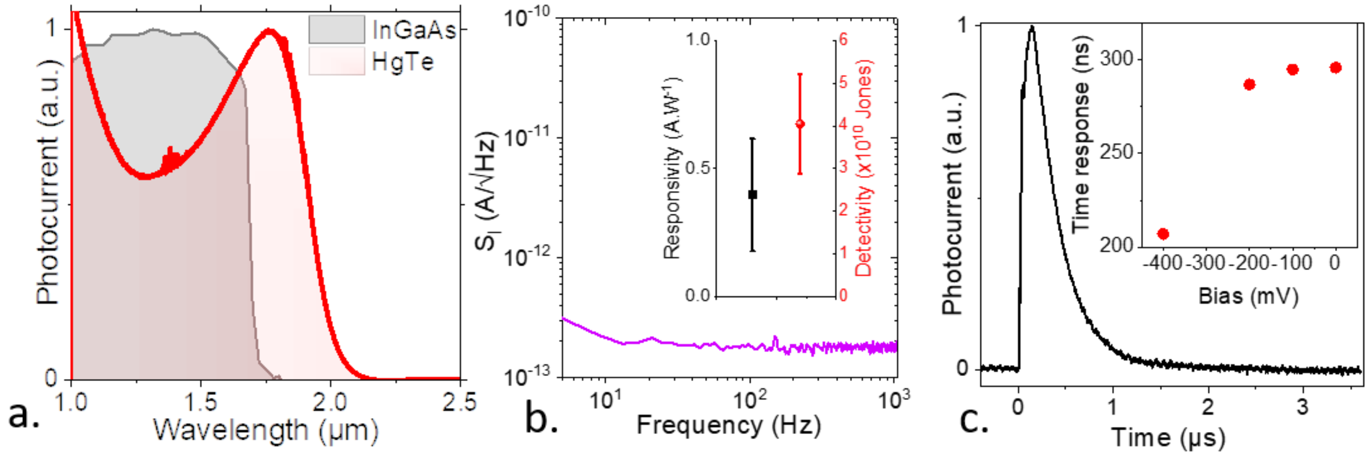

Figure 4 Performance of the FTO/doped:SnO_2/HgTe/Ag_2Te/Au stack. *a. Photoresponse spectrum of the diode compared with InGaAs alloy. b. Noise current spectral density as a function of the signal frequency for a diode with various sizes. The inset provides the responsivity (to a blackbody at 600 °C) and specific detectivity of the diode. The error bar corresponds to the standard deviation. d. Photocurrent at 0 V as a function of time while a 1 ns pulse of light at 1573 nm illuminates arriving at t=0 on the device. The pixel size is 50 µm by 1 mm. Inset. Decay time of the temporal response as a function of the applied reverse bias.*

Figure 4 shows the performance of this diode. In **Figure 4**a, the spectral response has been measured and compared with the one of epitaxially matched InGaAs grown on InP. The diode presents a 2 µm cut-off wavelength (1.75 µm peak response), which genuinely expands the response toward longer wavelengths with respect to InGaAs. Under blackbody illumination (*i.e.,* broadband illumination), the measured response is in the range from 0.2 to 0.5 A.W^{-1}, with the best performing device exhibiting a response of 0.8 A.W^{-1}, see the inset of **Figure 4**b and S7. The typical external quantum efficiency is in the 20-30% range. Since the absorption is ≈1/3, this diode stack presents a high internal efficiency of 60-90 %, consistent with the determined diode band alignment. The response time of the diode (from exponential fit of the decay part of the curve) has been measured to be around 300 ns, see **Figure 4**c. The latter can be reduced to 200 ns under the application of a moderate reverse bias, see the inset of **Figure 4**c and S8.

A striking feature of this diode is the lack of *1/f* noise even at moderate signal frequency, see **Figure 4**b. The detectivity at room temperature and under 0 V operation falls in the 3-4 x10^{10} Jones (inset of **Figure 4**b, which is fairly competitive without being the best for HgTe-based diodes operating at this wavelength. Likely the device absorption is becoming a clear limitation to the diode performance, and introducing a light management strategy[35–40] would be a realistic next step to this work. A complete comparison of the diode performance is given in Table 1.

Table 1 Figures of merit relative to light sensors operating in the SWIR and based on HgTe NCs. (PC: photoconductive, PT: phototransistor, PD: photodiode)

Cut-off λ (µm)	**Operating mode**	**Responsivity** ($A.W^{-1}$)	**Response time**	**Detectivity** (jones)	**Operating temperature** (K)	**Specific feature**	**Ref.**
2.5	PC	0.1	10 µs	3.5×10^{10}	230	As_2S_3 surface chemistry	41
2.5	PC	1000	20 µs	2×10^{12}	200	Nanotrench	42
2.5	PC	150	1.5 ms	6×10^{8}	80	HgTe decorated graphene channel	11
2.4	PC	0.9	264 µs decay time	8×10^{9}	300	Spray coating with patterning	43
2.4	PC	0.22	2.2 ms	3.5×10^{8}	300	Multicolor pixel	44
2.5	PT	6.5×10^{-3}	10 µs	10^{9}	220	Graphene electrode	45
2.5	PT	2.0×10^{-3}	14 µs	10^{12}	30	STO gate+resonator	40
2	PT	<0.5	≈10 µs	3×10^{10}	300	SiO_2 back gate	46
2.4	PT	1	1.5 µs	10^{10}	300	Hybrid Polymer: HgTe	47
2.5	PT	-	15 ms	-	300	Doped-graphene/ HgTe	48
2.5	PT	0.08	10 µs	$>10^{8}$ $<10^{10}$	250	Planar pn junction based on dual gate	49
2.5	PD	2.5×10^{-3}	370 ns	3×10^{9}	300	HgTe ink	50
2.5	PD	0.25	260 ns decay time	3×10^{10} (without cavity) 7.5×10^{10} (with cavity)	300	Flexible substrate	23
2.2	PD	1	1.4 µs decay time	6×10^{10}	300	$HgCl_2$ treatment	21
1.8	PD	0.13	110 ns	2×10^{10}	300	With resonator	51
2.5	PD	0.6	-	4×10^{11}	85	Resonator grating + Fabry Pérot	18
2.4	PD	0.45	13 ns	10^{10}	300	Si/graphene/HgTe	52
2.5	PD	0.28	2.5 µs	6×10^{10}	300	Bi_2Se_3/HgTe/Ag_2Te	53

2	PD	0.3	300 ns	5x10^{10}	300	SnO_2/HgTe/Ag_2Te	**This work**

At this stage, the use of a top gold electrode still prevents the transfer of such a diode to a focal plane array. This is why we test the robustness of this diode stack toward a reversed fabrication where the metallic mirror is on the substrate while the top contact is semi-transparent. We fabricated the following diode stack glass/gold/SnO_2/HgTe/Ag_2Te/gold/ITO, see **Figure 5**a for a schematic of the diode. Though not so usual in silicon foundries, gold can easily be deposited as a top layer onto a ROIC and presents the advantage of a high thermal and chemical stability. The attempt to replace this layer with a lower work function such as silver leads to a layer without a shiny reflective aspect due to transformation of Ag to silver chalcogenides in the presence of HgTe NCs. The active part of the diode remains the same as the one depicted in the first part of this paper. The top contact is made of a very thin (few nm) layer of gold used for its appropriate work function. This layer is then further coated by ITO (50-60 nm) deposited by sputtering. The layer thickness is chosen so that the sheet resistance of the contact remains low while ensuring a good IR transparency. In this configuration, the I-V curve remains rectifying, and the open-circuit voltage presents the same magnitude as the non-reversed diode, see **Figure 5**b and c. The responsivity of the diode in the reversed configuration is slightly reduced to the 0.1-0.2 A.W^{-1} range.

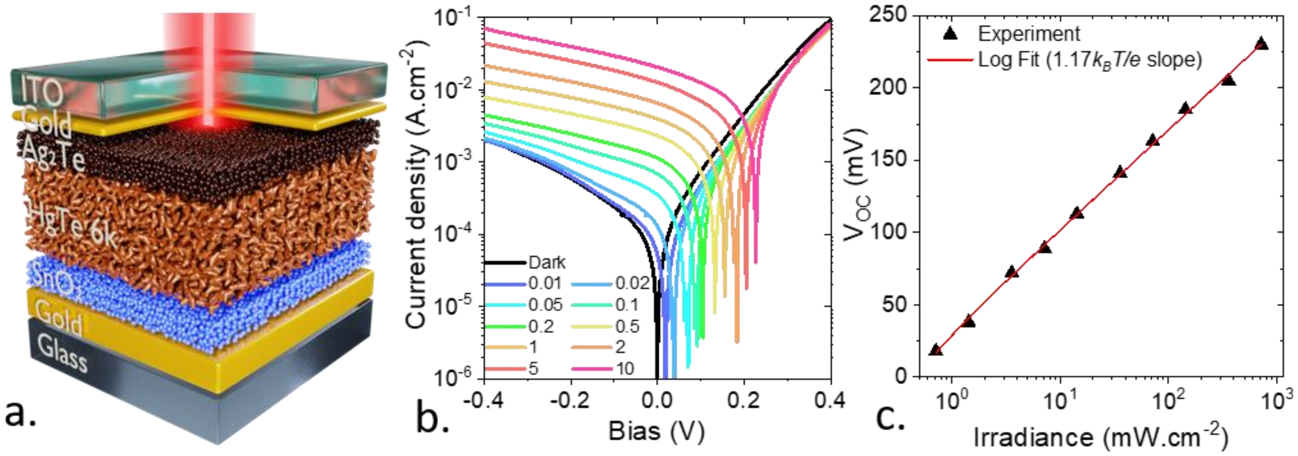

Figure 5 Reversed diode made of Au/doped:SnO_2/HgTe/Ag_2Te/Au/ITO stack *a. Schematic of the reversed diode based on the Au/doped:SnO_2/HgTe/Ag_2Te/Au/ITO stack. b. I-V curve in the dark and under illumination for the inverted diode at room temperature. c. Open-circuit voltage as a function of irradiance for illumination by a laser diode at 1.55 µm, for the reversed diode.*

To finish we have also tested the benefit of introducing this SnO_2 layer as electron injector while the diode is operated under forward bias to generate an electroluminescent signal. To confirm the presence of an electroluminescent signal we have image the LED under operation through a high pass filter that transmits photons above 1400 nm using an InGaAs camera (cut off wavelength 1.65 µm). As the diode is turned-on, we see a bright signal coming from the pixel, see Figure 6c and d. In this regime of operation, the I-V curve of the LED with and without the SnO_2 layer almost superimposed, see Figure 6a. However, the LED with the SnO_2 layer is typically 10 times brighter under low current, see Figure 6b.

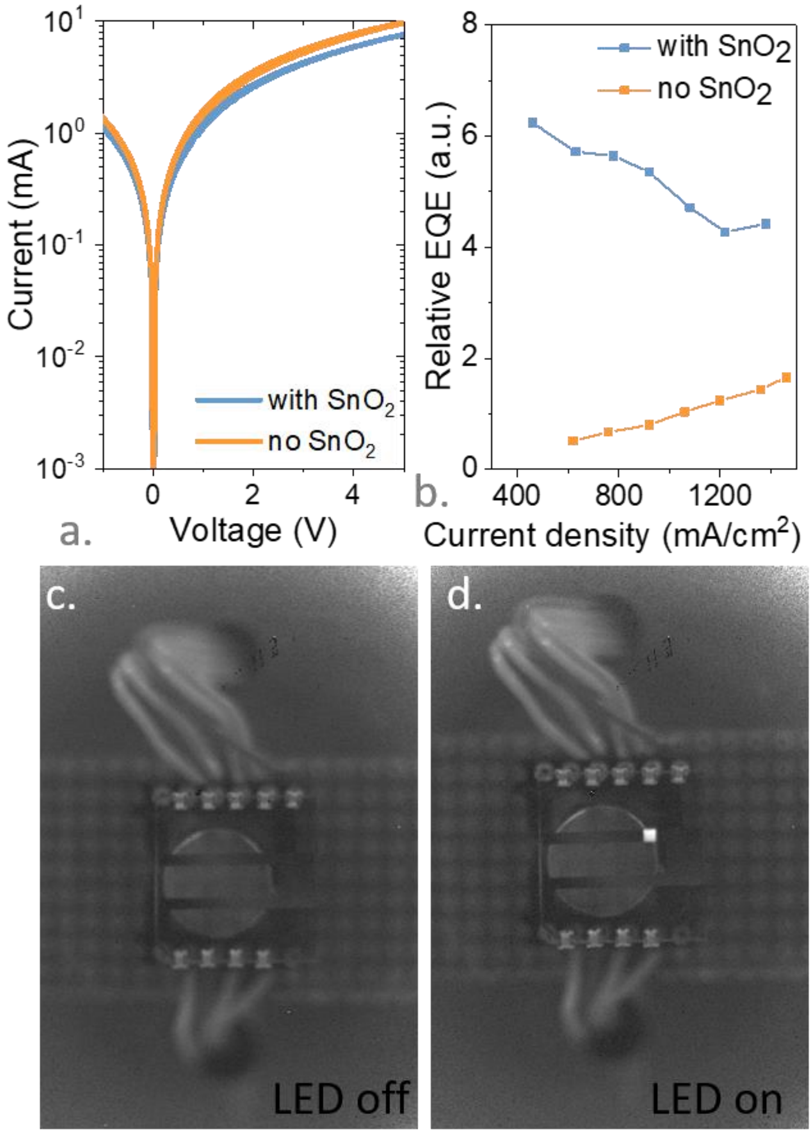

***Figure 6 Benefit of SnO$_2$ layer for electroluminescence**. a. IV curves of the LED stack with and without SnO$_2$ layer under forward bias. b. Relative EQE of the LED stack with and without SnO$_2$ layer under large forward bias. Image of the diode collected through a filter at 1.4 µm on a InGaAs camera while the LED is off (c.) and on (d.). The diode is operated at room temperature under 5 mA in this case.*

CONCLUSION

We demonstrate that SnO$_2$ is a well-suited electron extraction layer for HgTe NCs absorbing in the short-wave infrared. SnO$_2$ and HgTe present a nearly optimal band alignment that ensures an efficient filtering of the hole dark current while letting the photoelectrons flow. The resulting I-V curve presents an enhanced rectifying behavior including at room temperature. This band alignment enables a high internal efficiency in the 60 to 90% range. The diode performance is now limited by the diode absorption that will likely require the introduction of a light management strategy, although the device absorption is already increased compared to the free-standing layer. Another striking benefit of this diode stack is the absence of *1/f* noise which will limit the drift of the performance over time. We also have demonstrated that the diode is sufficiently robust to be reversed and that the performance is maintained while the diode stack is coupled with a partly transparent electrode. The next challenge is to transfer this structure onto a focal plane array to design a low-noise infrared imaging camera. Last, we have also shown that the introduction of the SnO$_2$ layer is benefitial to increase the electroluminescence signal.

Methods

Chemicals: Mercury chloride ($HgCl_2$, Sigma-Aldrich, 99%), **Mercury compounds are highly toxic. Handle them with special care.** Tellurium powder (Te, Sigma-Aldrich, 99.99%), silver nitrate (Alfa Aesar, 99.9%), SnO_2 nanoparticles (15% dispersion in water, Alfa Aesar), trioctylphosphine (TOP, Alfa Aesar, 90%), oleylamine (OLA, Acros, 80-90%), dodecanethiol (DDT, Sigma-Aldrich, 98%), ammonium chloride (Alfa Aesar, 98 %) ethanol absolute (VWR), methanol (VWR, >98%), isopropanol (IPA, VWR), hexane (VWR, 99%), octane (Carlo erba, 99%), 2-mercaptoethanol (MPOH, Merck, >99%), N,N dimethylformamide (DMF, VWR), N-methylformamide (NMF, Alfa Aesar, 99%), toluene (VWR, 99.8%). All chemicals are used without further purification except oleylamine that is centrifuged before use.

1 M TOP:Te precursor: In a three neck flask, we have mixed Tellurium powder (2.54 g) in 20 mL of trioctylphosphine. The flask is degassed under sub mbar pressure at room temperature for 5 min and then the temperature is increased to 100 °C. The degassing of the flask is conducted for 20 additional minutes. The atmosphere is switched to nitrogen and the temperature is raised to 275 °C. The solution turns to a clear orange coloration. The heating mantle is removed and the temperature of the flask cools down. Its color changes to yellow. Finally, this solution TOPTe is used as stock solution and stored into a glove box for storage.

HgTe NCs synthesis with band-edge at 6000 cm^{-1}: In a 50 mL three-neck flask, we have mixed 540 mg of $HgCl_2$ salt together with 50 mL of oleylamine. The flask is then degassed under reduced pressure at 110 °C. The solution is yellow and clear. Then, 2 mL of TOP:Te (1 M) are extracted from the glove box and are mixed with 8 mL of oleylamine. The atmosphere is replaced by nitrogen and the temperature tuned to 57 °C. The pre-heated TOP:Te solution is injected in the three neck flask and the solution turns dark after 1 min. After 3 min, we inject 10 mL of a mixture of 10% DDT in toluene and a water bath is used to prompt the drop of temperature. The content of the flask is split in 4 tubes and MeOH is added. After centrifugation, the pellets are redispersed using 10 mL of toluene in a single centrifuge tube. The solution is precipitated again using absolute EtOH. The formed pellet is redispersed in 8 mL of toluene. At this step, the NCs are centrifuged in fresh toluene to remove the lamellar phase. The solid phase is discarded by centrifugation and the supernatant filtrated.

Ag_2Te CQD synthesis: In a 50 mL three neck flask, 170 mg of $AgNO_3$ are mixed together with 25 mL of oleylamine and 2.5 mL of oleic acid. The flask is then degassed under vacuum at room temperature for 15 min and then at 70 °C for 10min. The atmosphere is replaced to nitrogen and 2.5 mL of TOP are added into the solution. Then, the temperature of the flask is raised to 160 °C. After 30 min, the solution becomes orange. At this step, 0.5 mL of TOP:Te (1M) is injected and the reaction is quenched after 10 min with a water bath. The crude solution was stored in a freezer at -20 °C. When needed, 800 µL of the unfrozen crude solution are precipitated with MeOH. After centrifugation the formed pellet is redispersed in a mixture containing 200 µL DDT and 600 µL of chlorobenzene. Then, the NCs are precipitated by addition of methanol. After centrifugation the pellet is dispersed using 800 µL of chlorobenzene. Again, the NCs are precipitated by addition of MeOH and centrifugation. The pellet is this time dispersed in 1.6 mL of a (9:1 volume ratio) mixture of hexane:octane.

SnO_2: The pristine solution (SnO_2-P) is obtained by diluting 400 µL of commercial solution with 0.8 mL of distilled water. For lightly doped SnO_2 (SnO_2-L), we dilute 200 µL of commercial solution with

1 mL of 24 mM NH_4Cl solution in water. For heavily doped SnO_2 (SnO_2-H), we dilute 200 µL of commercial solution with 1 mL of 48 mM NH_4Cl solution in water.

Infrared spectroscopy: we use a Thermo-Fischer iS50 in attenuated total reflection (ATR) mode. The spectra are averaged over 32 times and acquired with a 4 cm^{-1} resolution. To measure photocurrent spectrum, a Femto DLPCA 200 current amplifier, is used to bias and magnify the output current from the sample. The output signal is then fed into the FTIR electronics.

Transmission electron microscopy on NCs: A dilute NC solution is drop-casted onto a copper grid covered with an amorphous carbon film. This grid is degassed under secondary vacuum to reduce future contamination. A JEOL 2010F microscope, operated at 200 kV, is used for acquisition of pictures.

Electronic microscopy image on device: The TEM slice is prepared using a FEI Helios NanoLab600i dual beam SEM FIB fitted with an EasyLift micromanipulator for in situ lift-out. The ion column is operated at 30 kV for all the steps, except for final cleaning of the sample, for which tensions of 5 kV and 2 kV are used. The beam current varies in the 15 pA to 47 nA range. The electron beam is used to deposit a 20 nm thick carbon layer over an area of 20 µm x 2 µm. The ion beam is then used to deposit a 3 µm thick layer Pt over the same area. The slice is partially cut out and a Pt needle is fixed. The sample is lifted out in situ and then attached to a copper support grid. Thinning of the sample can then be processed using a gradual cross-section cleaning milling pattern, with a final milling beam current of 80 pA. Finally, the 5 kV and 2 kV cleaning steps are carried out on each side. The TEM images are performed with a JEOL probe corrected ARM200F TEM. The gun is a cold FEG used with a high voltage of 200kV. The slice is observed with a Gatan ultrascan 2kx2k Camera in TEM mode. The EDS spectrum and mapping used a CENTURIO-X SDD from JEOL. All the STEM images are done using BF and HAADF STEM detectors.

HgTe ink: We dissolve 30 mg of $HgCl_2$ salt in a solution of 2 mL of mercaptoethanol and 18 mL of DMF. This sokution is called exchange solution in the following of this paragraph. The solution of HgTe NCs is processed to obtain ligand exchange. At each step, the solution is stirred with a vortex and sonicated. 900 µL of HgTe NCs solution are mixed with 1 mL of the exchange solution. 5mL of hexane and 2 mL of DMF are added to the solution. The top phase is discarded, and the bottom solution is washed twice more adding 5 mL of hexane each time and removing the top phase every time. Then, toluene is added up to induce precipitation and the solution is centrifugated for 2 min at 6000 rpm. The supernatant is discarded and the formed pellet is dried under nitrogen flow. The dry pellet is then redispersed in 175 µL of DMF to reach a thickness of about $100\ \mathrm{nm}$. This solution is called ink. Before ink deposition, the substrate is placed in oxygen plasma cleaner for 2 min to promote adhesion. The ink is spin-coated on the substrate at 4000 rpm (at 2000 $rpm.s^{-1}$ acceleration) during 5 minutes. This gives a homogeneous deposit between 100 nm and 200 nm.

FTO etching: The surface of FTO coated (80 nm) glass (1.1 mm thick) substrate, purchased from Solems, is cleaned by sonication within an acetone bath. The substrate is rinsed with acetone, then isopropanol and dried using N_2 flow. A final cleaning is made using an O_2 plasma for 5 minutes. An adhesion primoter (Ti PRIME) is spin-coated on the cleaned substrate and baked for 2 min at 120 °C. AZ5214E resist is spin-coated and baked at 110 °C for 90 s. A standard photolithography process is performed using mask aligner for exposing the substrates to UV light for 20 s through a lithography mask. The resist is developed using AZ 726 developer for 30 s. reaction is stopped by dipping the sample into a deionized water bath. The sample is exposed one more time to an O_2 plasma to remove residual resists at the interface with the substrate. The FTO is then etched for 7 min using RIE, the etching gas is SF_6 (pressure: 7 mTorr, 25 sccm SF_6, Power = 70 W). After etching the resist is lift-off by dipping the film into acetone for a several hours. The film is finally rinsed with a flow of acetone and then isopropanol, before being dried under nitrogen flow.

Diode with FTO/doped:SnO_2/HgTe/Ag_2Te/Au stack: The FTO-coated glass substrates (see above procedure used to define patterns) are sequentially cleaned in acetone and isopropanol. The substrates are exposed to ozone plasma for 10 min. The SnO_2-L solution is deposited onto the patterned FTO substrate via spin-coating. The SnO_2-H solution is deposited onto the SnO_2-L layer. The film is annealed on a hot plate at 70 °C for 1h. The HgTe nanocrystals ink is deposited onto the SnO_2 film via spin coating. The thickness of the film is tuned with spin coating speed and ink concentration in DMF solvent. On top of HgTe ink film, Ag_2Te nanocrystals layer is spin-coated at 2000 rpm followed by $HgCl_2$ treatment. This layer is then cation exchanged, to do so we perform a a $HgCl_2$ treatment. 50 µL of $HgCl_2$ diluted in methanol (10 mM) is dropped onto HgTe film and spin-dried after 15 s. Then the film is rinsed using isopropanol. This procedure is repeated one more time. Finally, an ethanedithiol ligand-exchange is performed by dipping the film in a solution made of 1% ethanedithiol in acetonitrile for 30 s. The film is then rinsed with fresh acetonitrile. An top gold (80 nm) electrode is deposited with thermal evaporation under a vacuum of $\approx 5x10^{-6}$ mbar with a rate of 3 Å/s. To ensure a high degree of homogeneity, the substrate holder is spinned during the deposition.

Reversed photodiode based on Au/doped:SnO_2/HgTe/Ag_2Te/Au/ITO stack. We start with a glass substrate. The surface of the glass substrate (1.1 mm thickness) is cleaned by sonication in acetone. The substrate is rinsed with acetone, then isopropanol and dried with a N_2 gun. A final cleaning is made using an O_2 plasma. An adhesion primer (Ti PRIME) is spin-coated onto the substrate and baked at 120 °C for 2 min. AZ5214E is spin-coated and baked at 110 °C for 90 s. The substrate is exposed under UV through a pattern mask (the same as for FTO patterning) for 1.5 s. The film is then baked at 127 °C for 2 min in order to invert the resist. Then a 40 s flood exposure is performed. The resist is developed using a bath of AZ726 for 32 s and the sample is rinsed in pure water and dried with N_2. We then deposit 5 nm of chromium layer and 80 nm of gold layer using thermal evaporation. The lift-off is performed by dipping the film in acetone for 1 hour. The film is finally rinsed with a flow of acetone and then isopropanol, before being dried under nitrogen flow. The substrate is exposed to ozone plasma for 10 min. The SnO_2-L solution is deposited onto the patterned gold substrate via spin-coating. The SnO_2-H solution is deposited onto the SnO_2-L layer. The film is annealed on a hot plate at 70 °C for 1h. The HgTe nanocrystals ink is deposited onto the SnO_2 film via spin coating. The thickness of the film is tuned with spin coating speed and ink concentration in DMF solvent. On top of HgTe ink film, a Ag_2Te nanocrystals layer is spin-coated at 2000 rpm followed by $HgCl_2$ treatment. For $HgCl_2$ treatment, 50 µL of $HgCl_2$ methanol (10 mM) solution is dropped onto HgTe film and spin-dried after 15 s. Then the film is rinsed with isopropanol. This procedure is repeated one more time. Finally, an ethanedithiol ligand-exchange is performed by dipping the film in 1% ethanedithiol in acetonitrile solution for 30 s and rinsed with pure acetonitrile. A 3 nm Au layer is deposited with thermal evaporation under a vacuum of $\approx 5x10^{-6}$ mbar at the rate of 3 Å/s. Finally, 50-60 nm of ITO is deposited by sputtering from a PLASSYS (MP800S), the deposition speed is set at 0.36 $nm.s^{-1}$, a 0.4 Pa partial pressure of Ar (Ar flux=40 sccm) is used to generate the plasma and the radio frequency power is set to 1.1 $W.cm^{-2}$.

Photodiode characterization: The devices are operated in room conditions of pressure and temperature, unless specified. The sample is plugged in a sample holder that enable connexion of all pixel without further touching the diode. The sample holder is connected to a Keithley 2634 used as a source-meter that applied bias and measure current. For measurements under illumination, we use two types of sources: a blackbody (omega BB4B) typically operated at 600 °C used as a broad band source and a 1.55 µm laser diode. For the time-resolved measurements, we use a pulsed laser (CNI laser) at 1573 nm. The pulses are 1.2 ns long and repeated every 10 ms (100 Hz). A fast (<50 ps rise time) InGaAs photodiode is used to trigger the signal. An oscilloscope (Rohde & Schwarz, RTE 1102) acquires the outcoming signal through a 50 Ω resistor, which is proportional to I_{DS}.

Electroluminescence characterization: for EL the same diode stack as for the detector is used. The diode is biased using a Keitley 2400. The light signal is collected by an InSb detector cooled at nitrogen temperature. the relative EQE is the ratio of the photocurrent measurement on the InSb sensor divided by the current flowing within the diode. To image the diode, we used a VGA format InGaAs sensor (model 1601) from New Imaging technologies.

ASSOCIATED CONTENT

Supporting Information include (*i*) procedure and results for X-ray photoemission measurements, (*ii*) Field effect transistor fabrication and characterization, (*iii*) ellipsometry measurements and their use in RCWA simulation.

COMPETING INTEREST

The authors declare no competing financial interest.

ACKNOWLEDEGMENTS

We thank New Imaging technologies for providing the InGaAs camera. The project is supported by ERC starting grant blackQD (grant n° 756225). We acknowledge the use of clean-room facilities from the “Centrale de Proximité Paris-Centre” and the french RENATECH network. This work has been supported by the Region Ile-de-France in the framework of DIM Nano-K (grant dopQD). This work was supported by French state funds managed by the ANR within the Investissements d'Avenir programme under reference ANR-11-IDEX-0004-02, and more specifically within the framework of the Cluster of Excellence MATISSE and also by the grant IPER-Nano2 (ANR-18CE30-0023-01), Copin (ANR-19-CE24-0022), Frontal (ANR-19-CE09-0017), Graskop (ANR-19-CE09-0026) and NITQuantum (ANR-20-ASTR-0008-01), Bright (ANR-21-CE24-0012-02) and MixDferro (ANR-21-CE09-0029).

REFERENCES

(1) Rogalski, A. Progress in Quantum Dot Infrared Photodetectors. In *Quantum Dot Photodetectors*; Tong, X., Wu, J., Wang, Z. M., Eds.; Lecture Notes in Nanoscale Science and Technology; Springer International Publishing: Cham, **2021**; pp 1–74.

(2) Hafiz, S. B.; Scimeca, M.; Sahu, A.; Ko, D.-K. Colloidal Quantum Dots for Thermal Infrared Sensing and Imaging. *Nano Converg.* **2019**, *6*, 7.

(3) Pejović, V.; Georgitzikis, E.; Lee, J.; Lieberman, I.; Cheyns, D.; Heremans, P.; Malinowski, P. E. Infrared Colloidal Quantum Dot Image Sensors. *IEEE Trans. Electron Devices* **2021**, 1–11.

(4) Chu, A.; Martinez, B.; Ferré, S.; Noguier, V.; Gréboval, C.; Livache, C.; Qu, J.; Prado, Y.; Casaretto, N.; Goubet, N.; et al. HgTe Nanocrystals for SWIR Detection and Their Integration up to the Focal Plane Array. *ACS Appl. Mater. Interfaces* **2019**, *11*, 33116–33123.

(5) Buurma, C.; Pimpinella, R. E.; Ciani, A. J.; Feldman, J. S.; Grein, C. H.; Guyot-Sionnest, P. MWIR Imaging with Low Cost Colloidal Quantum Dot Films. In *Optical Sensing, Imaging, and Photon Counting: Nanostructured Devices and Applications 2016*; International Society for Optics and Photonics, **2016**; Vol. 9933, p 993303.

(6) Bossavit, E.; Qu, J.; Abadie, C.; Dabard, C.; Dang, T.; Izquierdo, E.; Khalili, A.; Gréboval, C.; Chu, A.; Pierini, S.; et al. Optimized Infrared LED and Its Use in an All-HgTe Nanocrystal-Based Active Imaging Setup. *Adv. Opt. Mater.* **2021**, 2101755.

(7) Chatterjee, A.; Pendyala, N. B.; Jagtap, A.; Rao, K. S. R. K. Uncooled Mid-Wave Infrared Focal Plane Array Using Band Gap Engineered Mercury Cadmium Telluride Quantum Dot Coated Silicon ROIC. *E-J. Surf. Sci. Nanotechnol.* **2019**, *17*, 95–100.

(8) Gréboval, C.; Chu, A.; Goubet, N.; Livache, C.; Ithurria, S.; Lhuillier, E. Mercury Chalcogenide Quantum Dots: Material Perspective for Device Integration. *Chem. Rev.* **2021**, *121*, 3627–3700.

(9) Zhang, S.; Hu, Y.; Hao, Q. Advances of Sensitive Infrared Detectors with HgTe Colloidal Quantum Dots. *Coatings* **2020**, *10*, 760.

(10) Liu, D.; Wen, S.; Guo, Y.; Yin, X.; Que, W. Synthesis of HgTe Colloidal Quantum Dots for Infrared Photodetector. *Mater. Lett.* **2021**, *291*, 129523.

(11) Grotevent, M. J.; Hail, C. U.; Yakunin, S.; Bachmann, D.; Calame, M.; Poulikakos, D.; Kovalenko, M. V.; Shorubalko, I. Colloidal HgTe Quantum Dot/Graphene Phototransistor with a Spectral Sensitivity Beyond 3 µm. *Adv. Sci.* **2021**, *8*, 2003360.

(12) Zhang, S.; Chen, M.; Mu, G.; Li, J.; Hao, Q.; Tang, X. Spray-Stencil Lithography Enabled Large-Scale Fabrication of Multispectral Colloidal Quantum-Dot Infrared Detectors. *Adv. Mater. Technol.* **2021**, 2101132.

(13) Goubet, N.; Jagtap, A.; Livache, C.; Martinez, B.; Portalès, H.; Xu, X. Z.; Lobo, R. P. S. M.; Dubertret, B.; Lhuillier, E. Terahertz HgTe Nanocrystals: Beyond Confinement. *J. Am. Chem. Soc.* **2018**, *140*, 5033–5036.

(14) Apretna, T.; Massabeau, S.; Gréboval, C.; Goubet, N.; Tignon, J.; Dhillon, S.; Carosella, F.; Ferreira, R.; Lhuillier, E.; Mangeney, J. Few Picosecond Dynamics of Intraband Transitions in THz HgTe Nanocrystals. *Nanophotonics* **2021**, *10*, 2753–2763.

(15) Guzelturk, B.; Trigo, M.; Delaire, O.; Reis, D. A.; Lindenberg, A. M. Dynamically Tunable Terahertz Emission Enabled by Anomalous Optical Phonon Responses in Lead Telluride. *ACS Photonics* **2021**, *8*, 3633–3640.

(16) Nam, M.; Kim, S.; Kim, S.; Jeong, S.; Kim, S.-W.; Lee, K. Near-Infrared-Sensitive Bulk Heterojunction Solar Cells Using Nanostructured Hybrid Composites of HgTe Quantum Dots and a Low-Bandgap Polymer. *Sol. Energy Mater. Sol. Cells* **2014**, *126*, 163–169.

(17) Günes, S.; Neugebauer, H.; Sariciftci, N. S.; Roither, J.; Kovalenko, M.; Pillwein, G.; Heiss, W. Hybrid Solar Cells Using HgTe Nanocrystals and Nanoporous TiO_2 Electrodes. *Adv. Funct. Mater.* **2006**, *16*, 1095–1099.

(18) Ackerman, M. M.; Tang, X.; Guyot-Sionnest, P. Fast and Sensitive Colloidal Quantum Dot Mid-Wave Infrared Photodetectors. *ACS Nano* **2018**, *12*, 7264–7271.

(19) Jagtap, A.; Goubet, N.; Livache, C.; Chu, A.; Martinez, B.; Gréboval, C.; Qu, J.; Dandeu, E.; Becerra, L.; Witkowski, N.; et al. Short Wave Infrared Devices Based on HgTe Nanocrystals with Air Stable Performances. *J. Phys. Chem. C* **2018**, *122*, 14979–14985.

(20) Jagtap, A. M.; Martinez, B.; Goubet, N.; Chu, A.; Livache, C.; Gréboval, C.; Ramade, J.; Amelot, D.; Trousset, P.; Triboulin, A.; et al. Design of Unipolar Barrier for Nanocrystal Based Short Wave Infrared Photodiode. *ACS Photonics* **2018**, *5*, 4569–4576.

(21) Ackerman, M. M.; Chen, M.; Guyot-Sionnest, P. HgTe Colloidal Quantum Dot Photodiodes for Extended Short-Wave Infrared Detection. *Appl. Phys. Lett.* **2020**, *116*, 083502.

(22) Gréboval, C.; Noumbé, U. N.; Chu, A.; Prado, Y.; Khalili, A.; Dabard, C.; Dang, T. H.; Colis, S.; Chaste, J.; Ouerghi, A.; et al. Gate Tunable Vertical Geometry Phototransistor Based on Infrared HgTe Nanocrystals. *Appl. Phys. Lett.* **2020**, *117*, 251104.

(23) Tang, X.; Ackerman, M. M.; Shen, G.; Guyot-Sionnest, P. Towards Infrared Electronic Eyes: Flexible Colloidal Quantum Dot Photovoltaic Detectors Enhanced by Resonant Cavity. *Small* **2019**, *15*, 1804920.

(24) Khalili, A.; Abadie, C.; Dang, T. H.; Chu, A.; Izquierdo, E.; Dabard, C.; Gréboval, C.; Cavallo, M.; Zhang, H.; Pierini, S.; et al. Colloidal II–VI—Epitaxial III–V Heterostructure: A Strategy to Expand InGaAs Spectral Response. *Appl. Phys. Lett.* **2022**, *120*, 051101.

(25) Nethercot, A. H. Prediction of Fermi Energies and Photoelectric Thresholds Based on Electronegativity Concepts. *Phys. Rev. Lett.* **1974**, *33*, 1088–1091.

(26) Ye, J.; Li, Y.; Medjahed, A. A.; Pouget, S.; Aldakov, D.; Liu, Y.; Reiss, P. Perovskite Solar Cells: Doped Bilayer Tin(IV) Oxide Electron Transport Layer for High Open-Circuit Voltage Planar Perovskite Solar Cells with Reduced Hysteresis. *Small* **2021**, *17*, 2170020.

(27) Yoo, J. J.; Seo, G.; Chua, M. R.; Park, T. G.; Lu, Y.; Rotermund, F.; Kim, Y.-K.; Moon, C. S.; Jeon, N. J.; Correa-Baena, J.-P.; et al. Efficient Perovskite Solar Cells via Improved Carrier Management. *Nature* **2021**, *590*, 587–593.

(28) Yi, H.; Wang, D.; Mahmud, M. A.; Haque, F.; Upama, M. B.; Xu, C.; Duan, L.; Uddin, A. Bilayer SnO2 as Electron Transport Layer for Highly Efficient Perovskite Solar Cells. *ACS Appl. Energy Mater.* **2018**, *1*, 6027–6039.

(29) Zhu, P.; Gu, S.; Luo, X.; Gao, Y.; Li, S.; Zhu, J.; Tan, H. Simultaneous Contact and Grain-Boundary Passivation in Planar Perovskite Solar Cells Using SnO_2-KCl Composite Electron Transport Layer. *Adv. Energy Mater.* **2020**, *10*, 1903083.
(30) Chen, Y.; Meng, Q.; Zhang, L.; Han, C.; Gao, H.; Zhang, Y.; Yan, H. SnO_2-Based Electron Transporting Layer Materials for Perovskite Solar Cells: A Review of Recent Progress. *J. Energy Chem.* **2019**, *35*, 144–167.
(31) Jiang, Q.; Zhang, X.; You, J. SnO_2: A Wonderful Electron Transport Layer for Perovskite Solar Cells. *Small* **2018**, *14*, 1801154.
(32) Liu, H.; Lhuillier, E.; Guyot-Sionnest, P. *1/f* Noise in Semiconductor and Metal Nanocrystal Solids. *J. Appl. Phys.* **2014**, *115*, 154309.
(33) Lai, Y.; Li, H.; Kim, D. K.; Diroll, B. T.; Murray, C. B.; Kagan, C. R. Low-Frequency (*1/f*) Noise in Nanocrystal Field-Effect Transistors. *ACS Nano* **2014**, *8*, 9664–9672.
(34) Keuleyan, S.; Lhuillier, E.; Guyot-Sionnest, P. Synthesis of Colloidal HgTe Quantum Dots for Narrow Mid-IR Emission and Detection. *J. Am. Chem. Soc.* **2011**, *133*, 16422–16424.
(35) Zhu, B.; Chen, M.; Zhu, Q.; Zhou, G.; Abdelazim, N. M.; Zhou, W.; Kershaw, S. V.; Rogach, A. L.; Zhao, N.; Tsang, H. K. Integrated Plasmonic Infrared Photodetector Based on Colloidal HgTe Quantum Dots. *Adv. Mater. Technol.* **2019**, *4*, 1900354.
(36) Chen, M.; Shao, L.; Kershaw, S. V.; Yu, H.; Wang, J.; Rogach, A. L.; Zhao, N. Photocurrent Enhancement of HgTe Quantum Dot Photodiodes by Plasmonic Gold Nanorod Structures. *ACS Nano* **2014**, *8*, 8208–8216.
(37) Chen, M.; Lu, L.; Yu, H.; Li, C.; Zhao, N. Integration of Colloidal Quantum Dots with Photonic Structures for Optoelectronic and Optical Devices. *Adv. Sci.* **2021**, *8*, 2101560.
(38) Tang, X.; Ackerman, M. M.; Guyot-Sionnest, P. Thermal Imaging with Plasmon Resonance Enhanced HgTe Colloidal Quantum Dot Photovoltaic Devices. *ACS Nano* **2018**, *12*, 7362–7370.
(39) Dang, T. H.; Vasanelli, A.; Todorov, Y.; Sirtori, C.; Prado, Y.; Chu, A.; Gréboval, C.; Khalili, A.; Cruguel, H.; Delerue, C.; et al. Bias Tunable Spectral Response of Nanocrystal Array in a Plasmonic Cavity. *Nano Lett.* **2021**, *21*, 6671–6677.
(40) Gréboval, C.; Chu, A.; Magalhaes, D. V.; Ramade, J.; Qu, J.; Rastogi, P.; Khalili, A.; Chee, S.-S.; Aubin, H.; Vincent, G.; et al. Ferroelectric Gating of Narrow Band-Gap Nanocrystal Arrays with Enhanced Light–Matter Coupling. *ACS Photonics* **2021**, *8*, 259–268.
(41) Lhuillier, E.; Keuleyan, S.; Zolotavin, P.; Guyot-Sionnest, P. Mid-Infrared HgTe/As_2S_3 Field Effect Transistors and Photodetectors. *Adv. Mater.* **2013**, *25*, 137–141.
(42) Chu, A.; Gréboval, C.; Prado, Y.; Majjad, H.; Delerue, C.; Dayen, J.-F.; Vincent, G.; Lhuillier, E. Infrared Photoconduction at the Diffusion Length Limit in HgTe Nanocrystal Arrays. *Nat. Commun.* **2021**, *12*, 1794.
(43) Cryer, M. E.; Halpert, J. E. 300 nm Spectral Resolution in the Mid-Infrared with Robust, High Responsivity Flexible Colloidal Quantum Dot Devices at Room Temperature. *ACS Photonics* **2018**, *5*, 3009–3015.
(44) Cryer, M. E.; Browning, L. A.; Plank, N. O. V.; Halpert, J. E. Large Photogain in Multicolor Nanocrystal Photodetector Arrays Enabling Room-Temperature Detection of Targets Above 100 °C. *ACS Photonics* **2020**, *7*, 3078–3085.
(45) Noumbé, U. N.; Gréboval, C.; Livache, C.; Chu, A.; Majjad, H.; Parra López, L. E.; Mouafo, L. D. N.; Doudin, B.; Berciaud, S.; Chaste, J.; et al. Reconfigurable 2D/0D p–n Graphene/HgTe Nanocrystal Heterostructure for Infrared Detection. *ACS Nano* **2020**, *14*, 4567–4576.
(46) Abdelazim, N. M.; Zhu, Q.; Xiong, Y.; Zhu, Y.; Chen, M.; Zhao, N.; Kershaw, S. V.; Rogach, A. L. Room Temperature Synthesis of HgTe Quantum Dots in an Aprotic Solvent Realizing High Photoluminescence Quantum Yields in the Infrared. *Chem. Mater.* **2017**, *29*, 7859–7867.
(47) Dong, Y.; Chen, M.; Yiu, W. K.; Zhu, Q.; Zhou, G.; Kershaw, S. V.; Ke, N.; Wong, C. P.; Rogach, A. L.; Zhao, N. Solution Processed Hybrid Polymer: HgTe Quantum Dot Phototransistor with High Sensitivity and Fast Infrared Response up to 2400 nm at Room Temperature. *Adv. Sci.* **2020**, *7*, 2000068.
(48) Tang, X.; Lai, K. W. C. Graphene/HgTe Quantum-Dot Photodetectors with Gate-Tunable Infrared Response. *ACS Appl. Nano Mater.* **2019**, *2*, 6701–6706.

(49) Chee, S.-S.; Gréboval, C.; Magalhaes, D. V.; Ramade, J.; Chu, A.; Qu, J.; Rastogi, P.; Khalili, A.; Dang, T. H.; Dabard, C.; et al. Correlating Structure and Detection Properties in HgTe Nanocrystal Films. *Nano Lett.* **2021**, *21*, 4145–4151.

(50) Martinez, B.; Ramade, J.; Livache, C.; Goubet, N.; Chu, A.; Gréboval, C.; Qu, J.; Watkins, W. L.; Becerra, L.; Dandeu, E.; et al. HgTe Nanocrystal Inks for Extended Short-Wave Infrared Detection. *Adv. Opt. Mater.* **2019**, *7*, 1900348.

(51) Rastogi, P.; Chu, A.; Dang, T. H.; Prado, Y.; Gréboval, C.; Qu, J.; Dabard, C.; Khalili, A.; Dandeu, E.; Fix, B.; et al. Complex Optical Index of HgTe Nanocrystal Infrared Thin Films and Its Use for Short Wave Infrared Photodiode Design. *Adv. Opt. Mater.* **2021**, *9*, 2002066.

(52) Tang, X.; Chen, M.; Kamath, A.; Ackerman, M. M.; Guyot-Sionnest, P. Colloidal Quantum-Dots/Graphene/Silicon Dual-Channel Detection of Visible Light and Short-Wave Infrared. *ACS Photonics* **2020**, *7*, 1117–1121.

(53) Tang, X.; Ackerman, M. M.; Chen, M.; Guyot-Sionnest, P. Dual-Band Infrared Imaging Using Stacked Colloidal Quantum Dot Photodiodes. *Nat. Photonics 2019* **2019**, *13*, 277–282.

TOC graphic

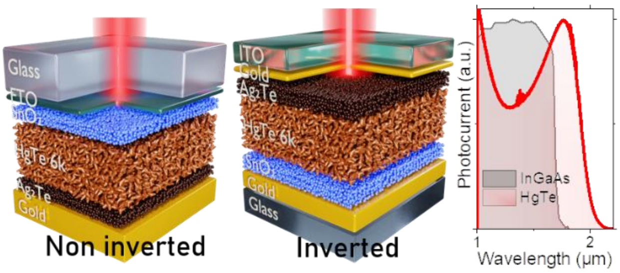
Glass
ITO
SnO2
HgTe 6k
Ag2Te
Gold
Non inverted
ITO
Gold
Ag2Te
HgTe 6k
SnO2
Gold
Glass
Inverted
Photocurrent (a.u.)
InGaAs
HgTe
1
2
Wavelength (µm)